Experimental Fluid Dynamic Characterization of Serrated Rotors for Drone Propulsion

Candeloro, Paolo; Nargi, Ranieri Emanuele; Grande, Edoardo; Ragni, Daniele; Pagliaroli, Tiziano

DOI
10.1088/1742-6596/1977/1/012007

Publication date
2021

Document Version
Final published version

Published in
Journal of Physics: Conference Series

Experimental Fluid Dynamic Characterization of Serrated Rotors for Drone Propulsion

Experimental Fluid Dynamic Characterization of Serrated Rotors for Drone Propulsion

Paolo Candeloro[1], Ranieri Emanuele Nargi[1], Edoardo Grande[2], Daniele Ragni [2], Tiziano Pagliaroli[1]

[1] Università Niccolò Cusano, Via Don Carlo Gnocchi 3, 00166 Rome, Italy
[2] Delft University of Technology, Delft, 2629HS, The Netherlands

E-mail: paolo.candeloro@unicusano.it

Abstract.

The present study reports an experimental investigation regarding one of the most effective and most studied passive control technique in literature to mitigate the noise pollution radiating by a small drone: the Serrated Trailing Edge (STE). 23 quiet propellers have been designed and manufactured in order to identify the most silent configuration. An aeroacoustic pre-qualification of the designed propellers has been performed by means of microphone measurements within the anechoic chamber of Niccolò Cusano University. Then, an aeroacoustic and fluid dynamic characterization of the most performing configuration has been carried out by means of load cell, microphone and PIV measurements in the anechoic wind tunnel facility of TUDelft University of Technology in order to investigate the mechanism that stands behind the noise mitigation. With this purpose, the aerodynamic and aeroacoustic performance and even the velocity and vorticity field along the blade of STE propellers have been characterized. Particular attention is devoted to the fluid-dynamic aspects related to the low Reynolds number flow regime. Results show that serrations seems to modify the wake velocity and the tip voretx intensity resulting in a lower acoustic emission.

1. Introduction

Drones, usually referred as Unmanned Aerial Vehicles (UAVs) or Micro Aerial Vehicles (MAVs), are automatized vehicle with high manoeuvrability in both hovering and cruise operations tipically designed with vertical or horizontal take-off and landing capabilities, and can manoeuvre with extremely high versatility and speed. Due to their unique properties of versatility for different tasks the contexts where drones find possible application are manifold. Actually, MAVs are widely employed for military aims, for example for tactical surveillance missions or for reconnaissance purposes, as well as in civilian applications as aerial crop surveys, medical supplies delivery, fire and large-accident investigation, infrastructure inspections, goods delivery and e-commerce. The use of small drones opens new possibilities in several application fields and this could have an enormous socioeconomic impact in the near future [1]. Regardless of the specific field of use, the noise produced by UAVs is one the key aspect which is slowing down the widespread deployment of these vehicles in urban areas. Even the Wall Street Journal indicates, in an article publisched in 2018 "Delivery Drones Cheer Shoppers, Annoy Neighbors, Scare Dogs" [2], Drone noise pollution as the main obstacle to widespread public acceptance of this technology in residential areas.

The scientific community's interest in the topic is demonstrated by the European Union *U-space* project. U-space is the set of services designed to regulate the safe and efficient access of drones into the airspace under $150\,m$. This would facilitate any kind of routine mission in all classes of airspace and all types of environment. The interest on the topic is due to the fast growth of drones technology in the last ten years and because in the future it is expected that this technology will be widely used in sectors such as logistics and healthcare. It is precisely to these two sectors that the operators pay special attention, since they will offer services in a complex context such as the urban one.
Furthermore, the main companies are working to move the urban mobility into airspace, this is the concept of Urban Air Mobility (UAM). It is estimated that by 2030 60% of the world's population will be urban. This significant population growth is expected to create a real need for innovative mobility options as ground infrastructure becomes increasingly congested. Providing people with a safe, sustainable and convenient solution that leverages the airspace above cities could be a solution. EASA in the Drones Amstedam Declaration 2018 recognized the social need for smarter mobility to improve quality of life. Such declaration encourage the European community to develop the public and infrastructural conditions for smart mobility solutions and that drones are an integral part in this scenario.
Generally, the electric propulsive system of a UAV is composed of the propeller, the brushless electric motor (which strongly reduce the mechanical noise), the energy source (i.e. batteries) [3]. Most of the noise produced can be associated with the engine and propeller. Since, in the last few years the noise reduction of the propulsive system, with a special focus on the propeller, has been a very interesting topic in the literature: [4] [5] [6] [7] [8] [9] [3] [10] [11] [12] [13] are just some examples. However, few studies have focused on low–Reynolds small-scale propellers. The main goal in propeller design process are, conventionally, the noise impact redution and the increase of flight endurance in order to achieve a strong growing of drones market. However, this is far from an easy task, in fact it is well know that endurance increase and noise reduction are contradictory goal. For these reasons, UAVs provide a great challenge for scientific community regarding noise characterization and prediction. Indeed, although the main noise sources are almost the same of helicopters applications, there are several unknown effects to investigate. Examples of interesting features deserving particular attention are the effect of size reduction and the balance between tonal and broadband noise. The main difference between small-scale and conventional propellers is the flight flow speed regime, identified by the Reynolds number at 75% span:

$$Re_c = \frac{0.75\, c\, \omega R}{\nu} \tag{1}$$

where c is the rotor blade chord, ω is the rotational regime, R is the rotor tip radius and ν is the air kinematic viscosity. Generally, for a full-scale helicopter, an indicative Re_c is about 10^6, instead for a UAV it may range from 10^4 to 10^5. In terms of conventional flat plate aerodynamics, the former Reynolds number explicates in a turbulent flow regime while the latter in a laminar-transitional flow regime [14]. This discrepancy calls into question the applicability of traditional noise prediction tools.
As already mentioned, propeller noise is a fundamental and challenging issue that can't be overlooked in the design process. Noise control strategies can be divided in two main categories: active and passive. The former have been widely used for large scale airfoils and propellers but these solutions are energy-consuming. On the other hand, passive flow control techniques enable the boundary layer to be manipulated without further consumption of external energy, and can be employed on small UAVs. For this reason, several research groups are focusing on passive control systems for noise reduction [15].
The idea for the proposed control strategy was inspired by the silent flight of owls [16][17][18]. The quietness of their flight is due to their characteristic wings, with three main physical fea-

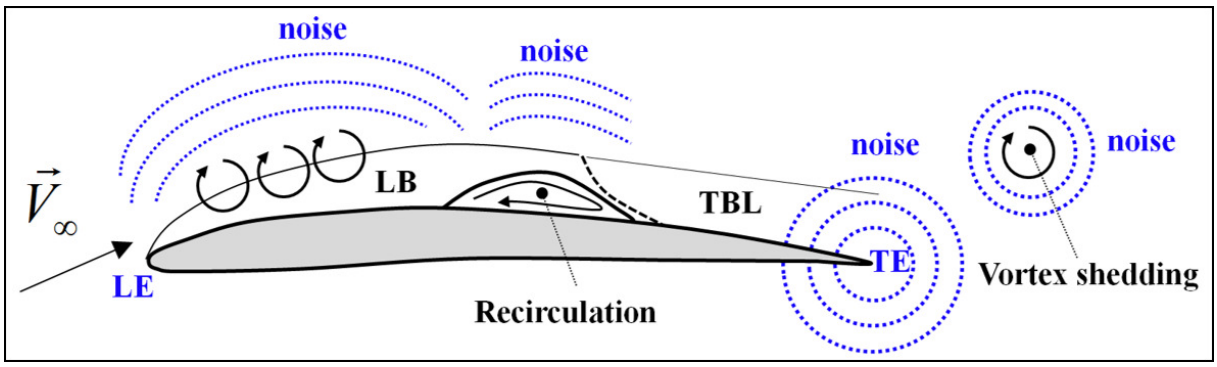

Figure 1. Representation of the main noise sources around an airfoil.

tures: a suction wing surface with a soft downy coating, a comb of stiff feathers at the wing leading edge, and TE feathers and wings with a fringe of flexible filaments. This original geometry represents the simplest way to mimic the permeability of owls' wings.
In this manuscript, The proposed control system is based on a sawtooth pattern employed at the TE of the blade. Serrations applied to the TE of an airfoil reduce noise generation due to the destructive interference of the pressure fluctuations produced by the flow structures convecting along the slanted edge.

2. Theoretical Background

This section provides a brief explanation of the most common noise prediction model (Sec.2.1), with a focus on the broadband component, and a short review of the study regarding the employment of serration already present in the literature (Sec.2.2).

2.1. Propeller noise modeling

The pressure fluctuation field $p'(\mathbf{x},t)$ radiating from a propeller can be divided into two main components in the Fourier domain: narrow (or tonal) and broad-band contributions [5][19][20][12]:

$$p'(\mathbf{x},t) = p'_{NB}(\mathbf{x},t) + p'_{BB}(\mathbf{x},t) \tag{2}$$

where $p'_{NB}(\mathbf{x},t)$ is the narrow-band component, whereas $p'_{BB}(\mathbf{x},t)$ is the broad-band counterpart.
Narrow (or tonal) components are directly related to the periodic motion of the blade in the surrounding fluid. Therefore, the radiated noise presents a frequency and magnitude connected to the rotational velocity of the propeller. The tonal components, for thin blades and low Mach numbers ($M < 1$), is given by the sum of a sound source related to blade thickness p'_T and one to aerodynamic loading p'_L:

$$p'_{NB}(\mathbf{x},t) = p'_T(\mathbf{x},t) + p'_L(\mathbf{x},t) \tag{3}$$

The thickness term takes into account the fluid displacement due to the body, whereas the loading counterpart takes count of the unsteady force distribution over the body surface.
Moreover, the propeller broad-band noise component is related to the interaction of turbulent flow structures with the blade edge. Thus, it is either generated at the blade leading/trailing edge or at the blade tip, and it is generally produced by three main sources: *i)* noise related to the turbulence of the incoming flow (*LE noise* p'_{LE}); *ii)* noise produced by the interaction of the turbulent boundary layer over the blade surface with the trailing edge (*TE noise*p'_{TE}) and *iii)*

noise generated by the possible separation of the flow (*Separation noise* p'_S) [5][13].
Therefore, the broad-band contribution can be further split as:

$$p'_{BB}(\mathbf{x},t) = p'_{TE}(\mathbf{x},t) + p'_{LE}(\mathbf{x},t) + p'_S(\mathbf{x},t) \tag{4}$$

The prediction of trailing edge noise has been subject of several study in the literature. Sinibaldi et al.[5] reports a relation between the Power Spectral Density at the trailing edge, S_{pp}^{TE}, and the spanwise fluid-dynamic correlation length, l_y:

$$S_{pp}^{TE}(r,\theta,\omega) = \frac{B}{8\pi}\left(\frac{\omega c}{2ar}\right)^2 \Delta R\, D(\theta,\phi)\, |I|^2\, \Phi_{pp} l_y \tag{5}$$

where r is the observer position vector, $\omega = 2\pi f$ is the angular frequency, f is the rotational frequency, B is the number of the blades, c is the chord, a is the speed of sound, ΔR is the spanwise length of the blade, $D(\theta,\varphi)$ is the directivity function, I is the radiation integral function, th operator $|\,|^2$ is the square of the absolute value and Φ_{pp} is the wall power spectral density of the pressure fluctuations.
There are different models to evaluate S_{pp}^{TE}, *e.g.* the one proposed by Schklinker and Amiet [21], or the more recent one proposed by Rozenberg et al. [22], which takes into account the effect of the adverse pressure gradient. Furthermore, l_y is usually estimated by means of the Corcos' model [23].
The noise control strategy analyzed and hereafter described is based on the model proposed in eq.5. More specifically, since $S_{pp}^{TE} \sim l_y$, a significant reduction of l_y, provided by varying TE geometry, should correspond to a noise reduction in the far field.

2.2. Serrated Trailing Edge noise

This section describes the investigated noise control techniques, especially the physical mechanism that enables noise reduction and the changes in aerodynamic performance induced by the noise control system itself.
To ensure that the mitigation of propeller noise is effective, the geometrical serration must obey three geometrical constraints: *i)* the dimensionless tooth height, defined as the ratio between the tooth half-height and the boundary layer thickness, $h^* = h/2\delta$, must be bigger than 0.25, otherwise the serration height is too small to have an interaction with the larger eddies convected into the boundary layer; *ii)* the serration angle, α (see fig.2(c)), must be smaller than 45°, to obtain a sharp saw–teeth [24][25]. For the sake of clarity, latter condition is equivalent to $AR_t = 2b/h < 4$; *iii)* the Strouhal number, defined as the ratio between the boundary layer thickness and reference flow velocity, $St_\delta = f\delta/U$ must be grater than one, as stated by Howe's theory for significant noise reduction.
The effect of serration on the aeroacoustics and aerodynamics of propeller, with particular attention to the influence on noise, thrust and torque generation, has been currently investigating and discussing by scientific community. For example, Intravartolo et al.[20] carried out an experimental analysis on serrated TE showing that an increase in serration height produces a reduction in the intensity of the TE wake. Nevertheless, benefits from the serrations height diminished with respect to the propeller overall noise signature. Moreover, if serration are not designed properly an increase in the overall noise may occur due mainly to aerodynamic effects. Serration depth effect has been the subject also of Pagliaroli et al. [12]. The main focus is the broad-band noise component and the directivity of the noise source in the near-field. A notable reduction in the noise generated was obtained in the low frequency region and a damping in the tails of the Probability Density Function (PDF) was observed. Such effect may give an interpretation about the physical phenomenon that lies behind the noise reduction. PDF's tails are related to intermittent structures, since serrations seems to act on strong energetic events

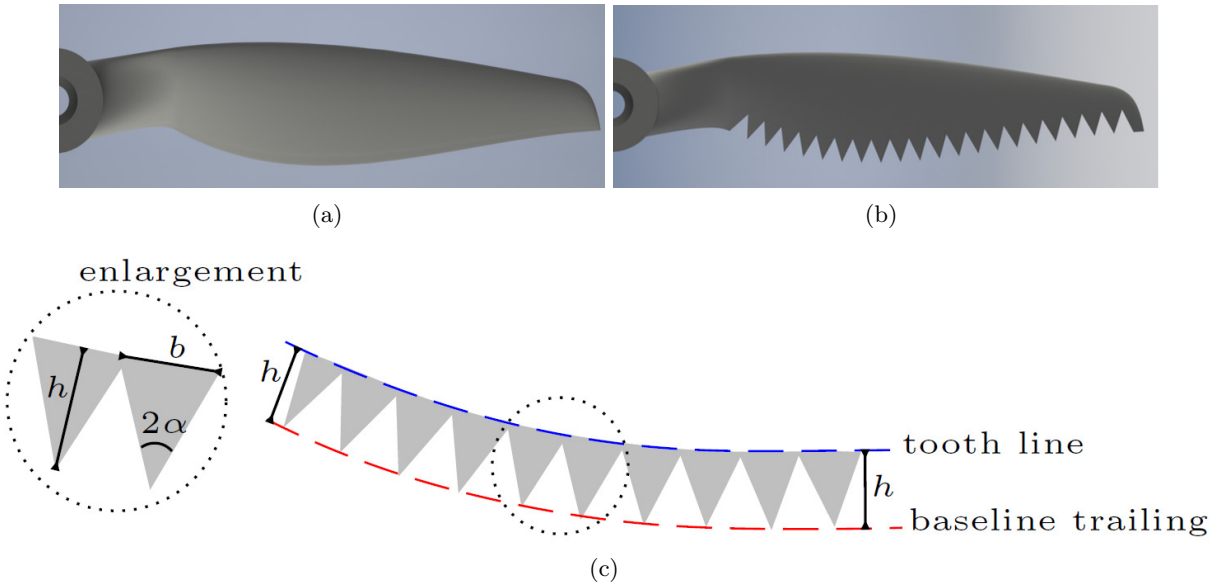

Figure 2. 3D rendering of the propeller blade: (a) baseline; (b) serrated trailing edge; (c) ketch of the serrated trailing edge. In the enlargement the main geometrical parameter of the tooth are reported: tooth basis b, height h and the serration angle α.

embedded in the pressure time series. Serrations drawback is a loss in aerodynamic efficiency, so the optimal geometry from both the acoustic and aerodynamic point-of-view must be found. Furthermore, the directivity pattern shows that STE effects are mostly bounded in the wake region. Candeloro et al. [13] demonstrate that if serrration are not designed properly they may even increase the noise generated by the propeller, since a particular care must be paid in the STE design process to guarantee a noise reduction.
Moreover, Halimi et al.[26][27] report an analytical study with the purpose of estimate the broadband noise spectrum of mini-drone to quantify the achievable noise reduction due to sawtooth trailing/leading edge. The innovative mathematical model was compared with the results of Lattice-Boltzmann based simulations. Results show that STE induce a noise reduction in the low and mid frequency region with the drawback of a noise increase in the high frequencies, noise reduction is more consistent when the serration sharpness grows up. The noise mitigation can be interpreted as a destructive scattering interference effect.

3. Methodology

3.1. Design of the STE propellers

Fig.2 reports a 3D rendering of two blades: one is a commercial blade (tyoe APC 9x4e) hereafter denoted as baseline (see Fig.2a), the other is the custom–made STE blade(see Fig.2b). All blades were obtained by removing material from the baseline to realize the different test cases: totally 23 propellers. Moreover, In Fig.2(c) the main geometrical serration parameters are reported: tooth height (h), width (b) and characteristic angle (α). In addition, a further parameter has been considered: the number of teeth n. Thus, for each geometry considered two propellers has been realized, one with $n = 10$ and one with $n = 5$. As mentioned in Sec.2.2, in the literature can be found constrains to achieve an acoustic effect. Therefore, the propeller were designed by keeping the $AR_t < 4$, that should guarantee a serration angle $\alpha < 45^{*\circ}$, as stated by [28]. The test cases are listed in Tab.1.

Case	b_i [mm]	h_i [mm]	n [−]	AR_t [−]	Marker
1	4	4	10	2	
2	4	3	10	2.66	
3	4	6	10	1.33	
4	4	8	10	1	
5	4	4	5	2	
6	4	3	5	2.66	
7	4	6	5	1.33	
8	4	8	5	1	
9	5	3	10	3.33	
10	5	6	10	1.66	
11	5	4	5	2.5	
12	5	3	5	3.33	
13	5	6	5	1.66	
14	6	4	10	3	
15	6	6	10	2	
16	6	8	10	1.5	
17	6	6	5	2	
18	6	8	5	1.5	
19	3	3	10	2	
20	3	6	10	1	
21	3	8	10	0.75	
22	3	6	5	1	
23	3	8	5	0.75	

Table 1. Test matrix of the preliminary measurement campaign, each study case corresponds to a propeller.

3.2. Experimental Setup

The aerodynamic, aeroacoustic and fluid-dynamic characterization has been performed within the A-tunnel facility of TUDelft University of technology. The A-Tunnel is a vertical, open-jet wind tunnel, where the surrounding of the nozzle exit consist of an anechoic chamber. A representation of the wind tunnel is reported in Fig.3. The nozzle is circular with a diameter D= 0.60 m. The propeller is connected to a profiled aluminium nacelle for minimum interference with the propeller flow, the instrumentations (composed by a motor, an encoder, a load cell and a torque cell) are embedded in the nacelle. The nacelle is supported by stiffened hollow aluminum NACA 0012 profiles of 0.06 m chord. The propeller is driven by an electrical brushless motor Leopard Hobby 3536-5T 1520 KV with a diameter of 27.8 mm and maximum power of 550 W. The motor is powered by a Delta Elektronika DC power supply. Rotor thrust is measured using a Futek LSB200 load cell excited with 5 VDC. Furthermore, the torque is measured using a Transducer Techniques RTS-25 torque sensor excited with 10 VDC. The thrust and torque signals are acquired by a National Instrument acquisition board with a sampling frequency of 5 kHz and an acquisition time of 30 s.

Moreover, far-field noise measurements has been carried by means of microphones semicircular array, centered at the propeller center, as sketched in Fig.3. The array has a radius of $r = 1.20\,m$ and is constituted by 4 LinearX M51 and 4 LinerarX M53 free field microphones. The Data Acquisition System (DAS) consisted of two National Instrument modules NI9234. A polar reference system has been adopted to define the angular position of each microphone with respect to the propeller center. Microphone voltages have been recorded for a duration of 30 s with a sampling frequency $f_s = 51200\,Hz$.

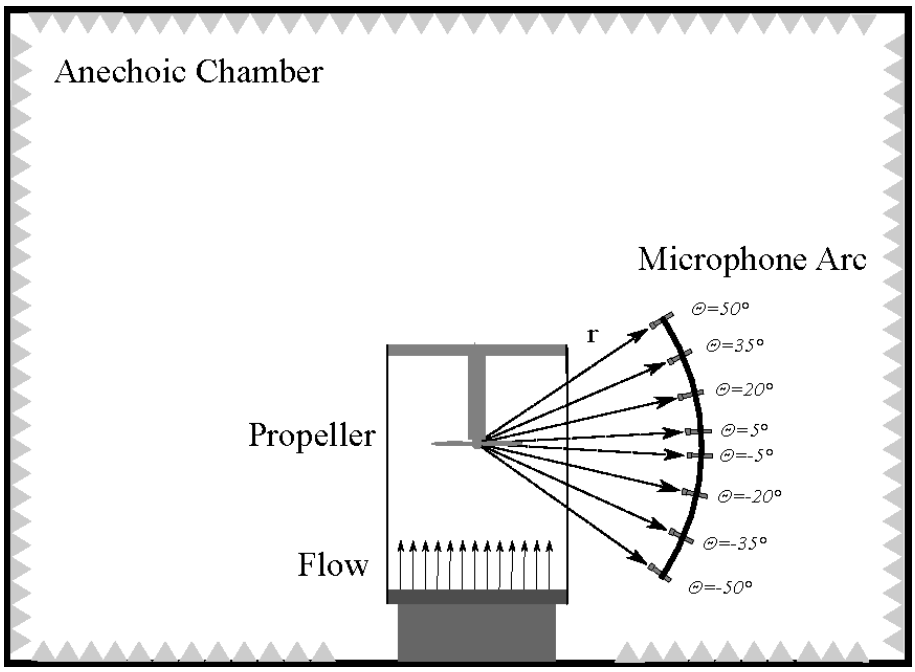

Figure 3. Sketch of the experimental setup employed for the microphones measurements campaign.

Finally, a stereoscopic PIV investigation has been conducted to investigate the propeller slipstream. Sets of 500 images have been recorded. The flow is seeded with particles of 1 micron median diameter produced by a SAFEX Twin Fog generator with SAFEX-Inside-Nebelfluid, a mixture of dyethelene glycol and water. The particles are introduced in the wind tunnel circuit to ensure a uniform concentration while recirculating. Illumination of the field of view is provided by a double cavity Quantel EVerGreen EVG00200 Nd:YAG laser with 200 mJ/pulse energy. A schematic representation of the stereoscopic PIV setup is shown in Fig.4. It can also seen how the laser beam is generated and converted into a laser sheet of 2 mm through light optics. The laser sheet is aligned with the propeller axis of rotation. Two Imager sCMOS camera with 2560 x 2160 pixels and four Nikon lenses with 50 mm focal length at f# 8 have been used for the measurements. In order to align the measurement plane with the focal plane, Scheimpflug adapters have been mounted on each camera. The camera calibration, acquisition and post-processing have been carried out with the LaVision Davis 8.4 software. The images are processed with a window deformation iterative multi-grid with a final interrogation window size of 16 x 16 pixels and 50% overlap. Spurious vectors are isolated through a median filter and replaced by interpolation. Details of the PIV setup apparatus are given in Tab.2-3.

4. Results

4.1. Aeroacoustics Pre-Qualification

In this section, the obtained results are presented. As already mentioned, the first step of the study consists in an acoustic characterization of the manufactured propellers carried out within the anechoic chamber of Niccolò Cusano University. The aim of such activity was to identify the most interesting configurations in terms of acoustic emissions.

In order to evaluate the aspect ratio $AR_t = 2b/h$ effect, the OverAll Sound Pressure Level

Imaging Parameters	
Camera	2 Imager sCMOS
Number of pixels [px]	2560 x 2160
Pixel size [μm]	6.5 x 6.5
Focal length [mm]	50
Magnification	0.05
FOV [cm^2]	35 x 35
Imaging resolution [px/mm]	8

Table 2. Details of Imaging Parameters.

PIV Parameters	
Software	LaVision Davis 8.4
Pulse separation [μs]	10
Number of recordings	500
Windows size [px^2]	16 x 16

Table 3. Details of PIV Parameters.

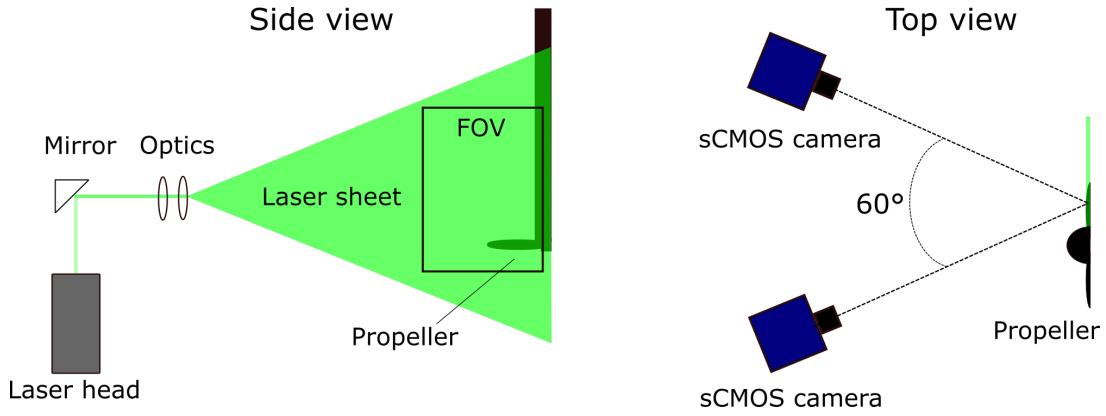

Figure 4. Stereoscopic PIV setup: (left) side view, (right) top view.

($OASPL$) of each rotor was calculated. The OASPL is defined as:

$$OASPL = 10 \log_{10} \left(\frac{\langle p'^2 \rangle}{p_{ref}^2} \right) \tag{6}$$

where $\langle \cdot \rangle$ denotes an ensemble average and $p_{ref} = 2 \times 10^{-5} Pa$ is the reference pressure (threshold of human hearing).
The results are reported in Fig.5; each point corresponds to a different propeller (for the test cases see Tab.1). In addition, a red dotted line, which represents the baseline propeller, was added to each plot as reference. The OASPL is representative of the total energetic content of the pressure time series and, in this sense, may give us global information about the propeller noise impact. Results show that the noise source presents a strong directivity, in particular it is interesting to underline that serration seems to act when the polar angle θ (see Fig.3) exceed a value of 0° (fig.5(d)). In this case, the experimental points obtained for almost all propellers are located under the red dotted line, that can be interpreted as a lower acoustic impact. This feature suggests that STE effects may be confined in the propeller wake region. Moreover, from these plots appears clear that if STE are not designed properly they may even cause an increase

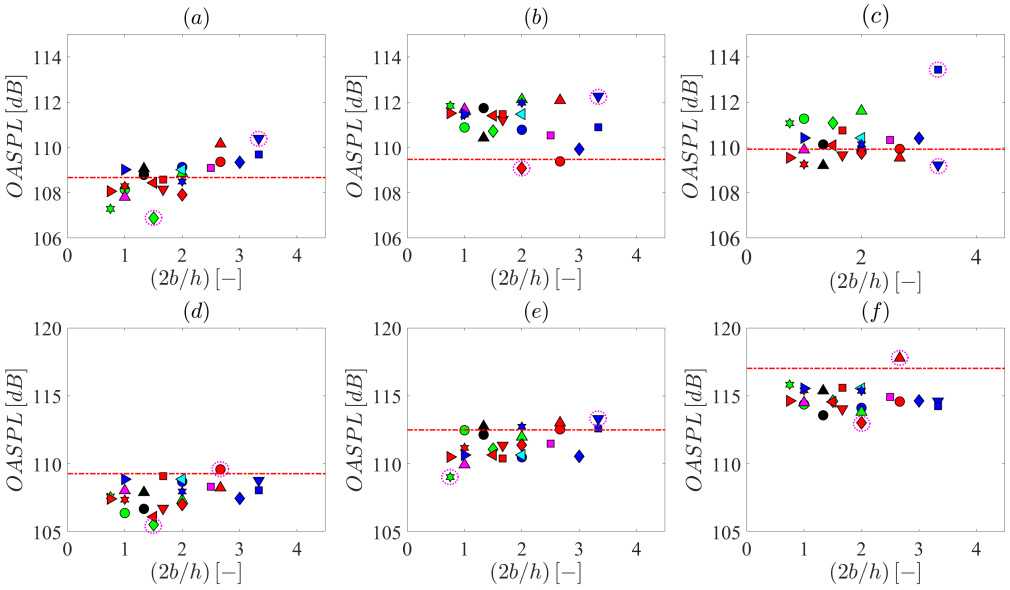

Figure 5. SPL trend for each blade at rotational velocity $\Omega = 4000\,RPM$ by varying the polar angle θ. (a):$\theta = -90°$ (b):$\theta = -60°$ (c):$\theta = -30°$ (d):$\theta = 0°$ (e):$\theta = 30°$ (f):$\theta = 60°$

in the noise impact. Such effect makes the parametric study fundamental to design serration that guarantee a suitable acoustic feature. Finally, for each test cases the best and worst propeller has been highlighted with a red circle; between these test cases the main interesting propellers has been identified and employed for the fluid dynamic characterization. The chosen propellers correspond to the test case 6, that presents the worst aeroacoustic behaviour, and 15, corresponding to the best aeroacustic properties. Tab.1) reports their geometrical parameters. In the following to define such propellers they will be called b_1h_2 and b_3h_3 respectively.

4.2. Aerodynamic and Aeroacoustic Results

Subsequently, an aerodynamic and aeroacoustic characterization of these 2 propeller, and also of the reference one, has been carried out. From the literature it is know that noise emission and thrust generation are contradictory goal since it is fundamental to find a compromise solution. Therefore, the thrust coefficient c_T has been calculated, this dimentionless coefficient, for rotor, is generally defined as [29]:

$$c_T = \frac{T}{\rho n^2 D^4} \tag{7}$$

where T is the thrust in N, ρ the air density kept constant at $1.225\,kg/m^3$, n the rotational frequency expressed in $1/s$, D the rotor disk diameter in m. Results obtained for the hovering condition by varying the propeller rotational velocity Ω in the range $[2000 : 6000]$ RPM, typical for drones applications, are reported in Fig.6(a) indicating an evident lowering of the c_T, mostly regarding the b_3h_3 propeller. Such results confirm what found in [20, 12, 13] that a longer tooth length induce a major thrust loss. However, Eq.7 is the classical formulation employed for rotor but it does not take into account the surface difference between the three propellers. For this reason, in the present study, also an alternative formulation has been considered in order to quantify the serration effect related to flow modification. For this purpose, the thrust force T

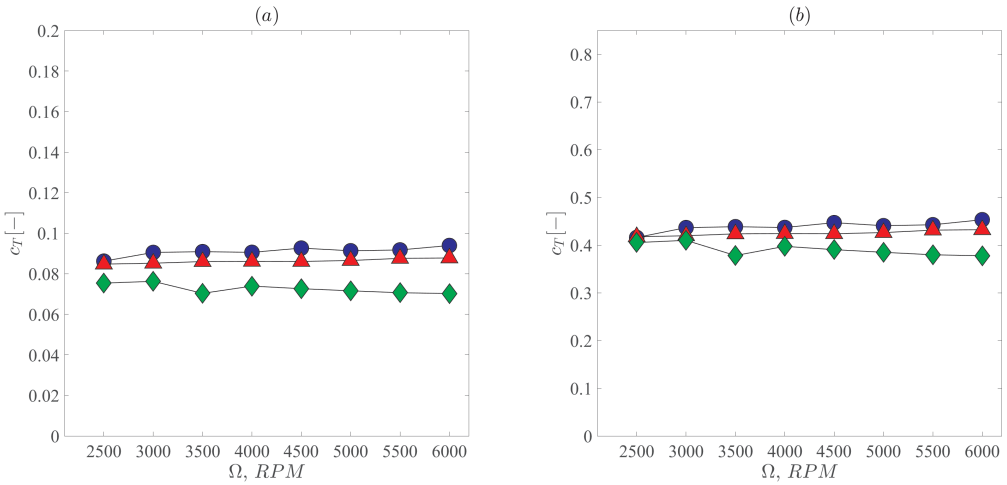

Figure 6. Thrust coefficient c_T(a) and $\tilde{c}_T$(b) trend by varying the rotational velocity Ω in hovering flight condition. The $\circ$ represents the baseline propeller, the $\triangle$ the b_1h_2 propeller and the $\diamond$ line the b_3h_3 propeller.

was normalized by the dynamic pressure $\frac{1}{2}\rho V^2$ [30] and it is possible to define a $\tilde{c}_T$:

$$\tilde{c}_T = \frac{T}{\frac{1}{2}\rho\widehat{S}V^2} = \frac{T}{\frac{1}{2}\rho\widehat{S}(\Omega R)^2} \tag{8}$$

where $\widehat{S}$ is the effective surface of the propeller. Thus, this formulation keep in count the reduction in the lifting surface due to the material removal for the sawtooth pattern manifacturing. Fig.6(b) reports the obtained results for $\tilde{c}_T$. As a result, the reduction of thrust coefficient seems less evident and attributable in fewer than 10%.

The thrust coefficient has been calculated even in the case of advanced flight at fixed rotational velocity $\Omega = 5000\,RPM$, the advance velocity v considered for experimental test are in the range $[0 : 9]\,m/s$, corresponding to an Advance Ratio $J = \frac{v}{nD} = [0 : 0.6]$. The results are in agreement with the previous one, a reduction of the thrust coefficient can be observed, in Fig.7(a) the results in term of c_T are reported showing a sensible reduction but, as in the case before, Fig.7(b) clarifies that just a few portion of it is directly connected to serration and a second part could be ascribed to the difference in the propeller surface.

In conclusion, serration seems to induce a loss in the propellers aerodynamic properties that is expected because of the modification of the shape of the propeller but must be taken into account in the design process. The experimental evidence is that the thrust is almost the $10-15\%$ lower than the baseline for hovering, reaching the $20-30\%$ in advanced flight. Such problem could be overcome by using add-on serrations.

Then, the $OASPL$ has been calculated and presented in the form of directivity map. Fig.8 reports the results at constant rotational velocity $\Omega = 5000\,RPM$ and different advance velocity: (a) $v = 0\,m/s$ $(J = 0)$, (b) $v = 3\,m/s$ $(J = 0.17)$, (c) $v = 6\,m/s$ $(J = 0.35)$. Both the hover and the advanced flight condition present a minimum noise emission at the rotor plane. Serration effect seems more evident for $v = 3\,m/s$ (Fig.8(b)), the b_3h_3 exhibits a strong reduction of

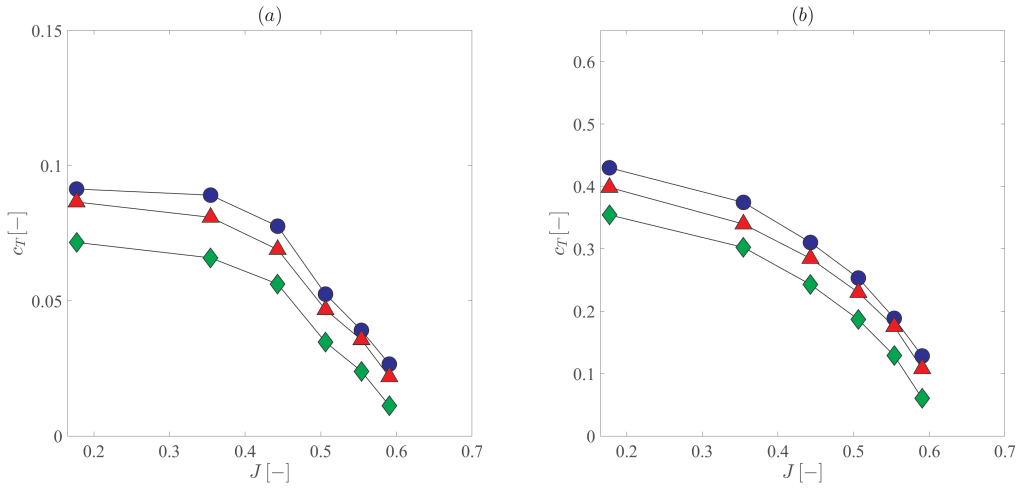

Figure 7. Thrust coefficient c_T(a) and $\tilde{c}_T$(b) trend by varying the advance ratio J . The $\circ$ represents the baseline propeller, the $\triangle$ the b_1h_2 propeller and the $\diamond$ line the b_3h_3 propeller.

$3-4\,dB$ whit respect to the baseline over the entire polar angle range, i.e. $-50° \leq \theta \leq 50°$. On the other hand, the b_1h_2 explicates almost the same noise impact of the baseline. Fig.8(c) shows that if the velocity grows both the STE propeller shows a reduction in the OASPL in respect to the baseline. Such results suggest that serration effect become more important for advanced flight condition. Furthermore, a preferential velocity for noise mitigation may be observed corresponding to $v = 3\,m/s$, especially for the b_3h_3 propeller. These behaviours needs to be further investigated in the future.
A spectral analysis has been carried out, that is not reported here for the sake of brevity, the main results are that noise reduction can be ascribed to both the tonal (probably related to thrust mitigation) and the broadband (main focus of this manuscript) component.

4.3. PIV Results
A stereoscopic PIV of the propellers (*Baseline*, b_1h_2, b_3h_3) slipstream has been carried out at constant rotational velocity $\Omega = 5000\,RPM$ and two values of advance velocity: $v = 0\,m/s$ (hover condition); $v = 6\,m/s$ ($J = 0.35$). The aim is to characterize the flow around the blade with a particular focus on the modification related to serration and to establish a relationship with the noise generation. Fig.10 reports on the first row the mean velocity and on the second row the rms velocity distributions in hover condition. The reference system is centered with the propeller center, the x and y axis are normalized with respect to the propeller radius and the flow is aligned with the y axis. The three propellers exhibit an increase of the axial velocity component downstream. Specifically, the baseline and b_1h_2 propellers present similar values of wake velocity while the b_3h_3 shows a lower values of this magnitude. Such effect are clarified in Fig.9, where are reported the mean velocity profiles for the three propellers at three different stations in the slipstream, respectively, $y/R = 0.5$ (a), $y/R = 1$ (b) and $y/R = 1.5$ (c). The b_1h_2 has the maximum of wake velocity almost identical to the baseline, whereas the b_3h_3 outcome a lowering about the 20% respect to the baseline. Moreover, serration seems also to modify the distribution of wake velocity in the spanwise direction. Indeed, the velocity maximum in

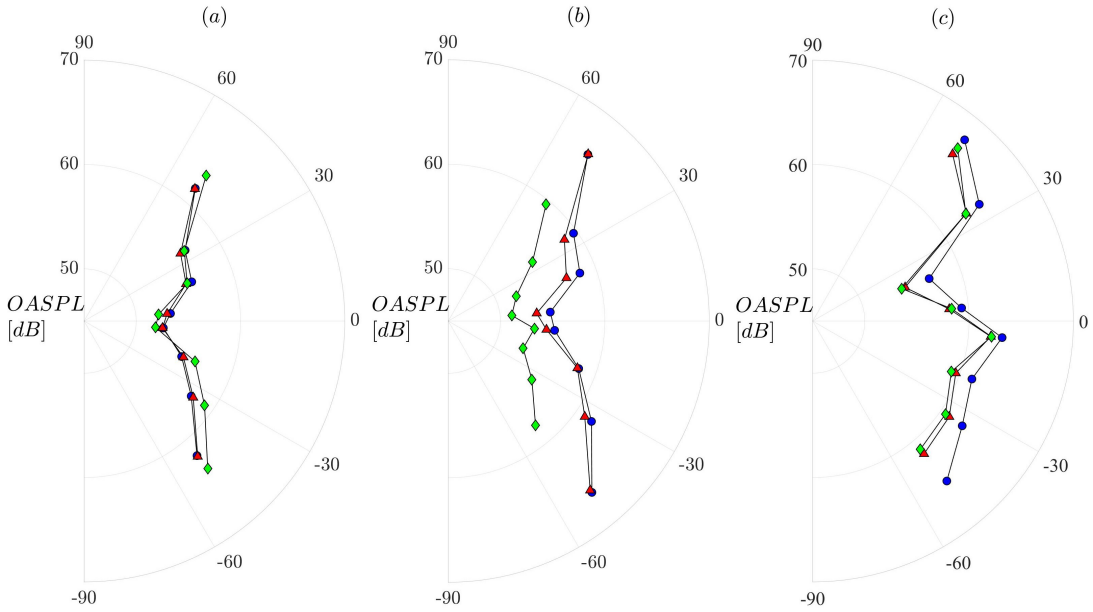

Figure 8. Directivity plot from the semicircular array of microphones at $\Omega = 5000\,RPM$ and $v = 0\,m/s$ (a), $v = 3\,m/s$ (b) and $v = 6\,m/s$ (c). The $\circ$ represents the baseline propeller, the $\triangle$ the b_1h_2 propeller and the $\diamond$ line the b_3h_3 propeller.

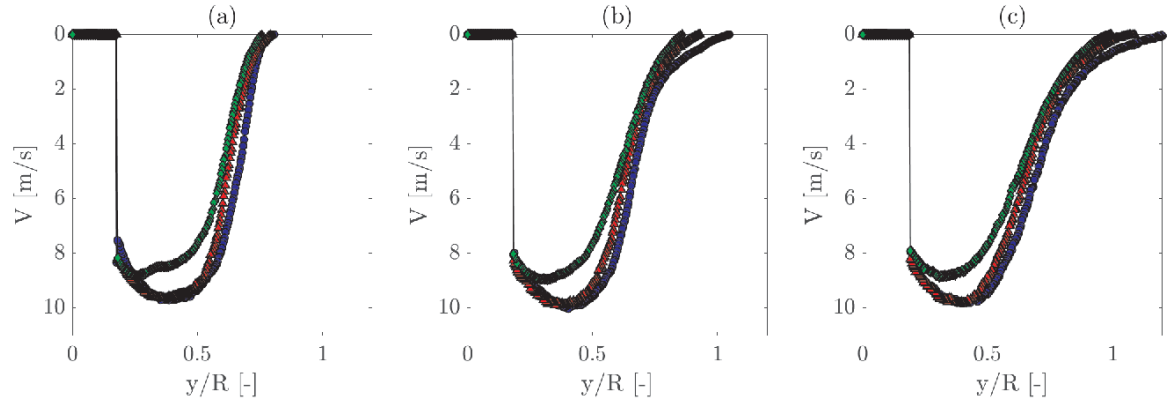

Figure 9. Mean velocity profiles at (a) $y/R = 0.5$, (b) $y/R = 1$ and (c) $y/R = 1.5$ for $v = 0\,m/s$ and $\Omega = 5000\,RPM$. The $\circ$ represents the baseline propeller, the $\triangle$ the b_1h_2 propeller and the $\diamond$ line the b_3h_3 propeller.

x direction is different for the b_3h_3 propeller respect to the b_1h_2 propeller and closer to the propeller root. The analysis of the rms velocity (second row of Fig.10) reveals that most of the velocity fluctuation are related to the tip vortex generation, which seems to be mitigated by the serrations. In addition, the b_3h_3 propeller induce a stronger mitigation than the b_1h_2, in fact the former presents a lower rms velocity in comparison to the latter. Seems evident that the tip vortex intensity of the b_3h_3 is much lower with respect to the baseline and, as it travel downstream, it is dissipated faster. This is not the case for the b_3h_3 propeller, where, at the same location, the tip vortex has lost most of his strength and mixed with the surroundings.

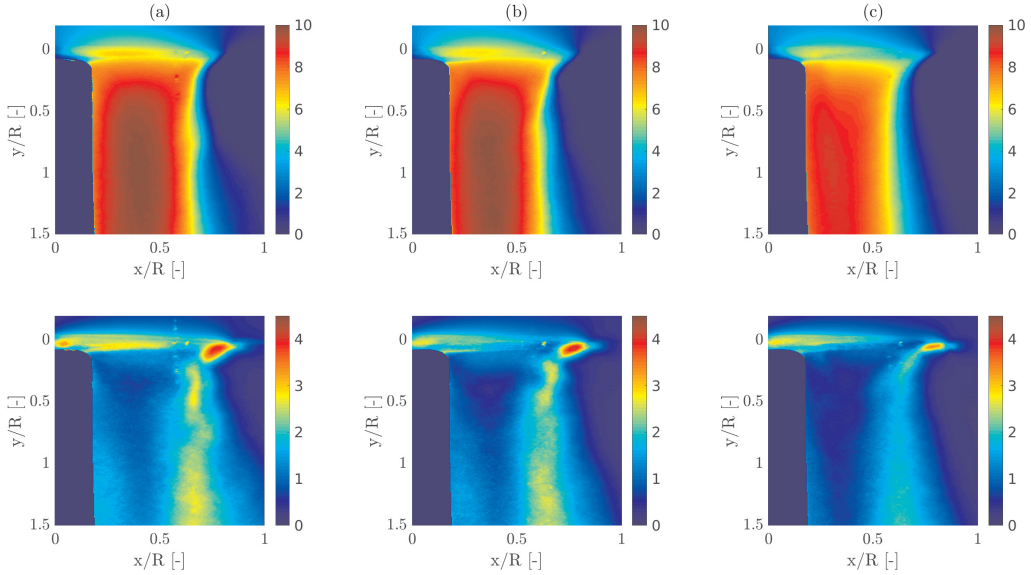

Figure 10. Mean velocity (top) and rms velocity (bottom) at $v = 0\,m/s$ and $\Omega = 5000\,RPM$. (a) represents the baseline propeller, (b) the b_1h_2 propeller and (c) the b_3h_3 propeller.

The results in the case of $v = 6\,m/s$ are reported in Fig.11, even in this figure the first row is the velocity mean field and the second row the velocity rms. Results are in agreement with the previous, or rather, the b_1h_2 propeller shows similar values of wake velocity compared to the baseline while the b_3h_3 presents a reduction of this quantity. The velocity profiles (see Fig.12) show that, even in this case, the effect of serration is two-fold: in the one hand, the maximum value of wake velocity has been mitigated (reduced of almost the 10% for the b_3h_3 in respect to the baseline); on the other hand, the distribution along the spanwise direction has been modified.

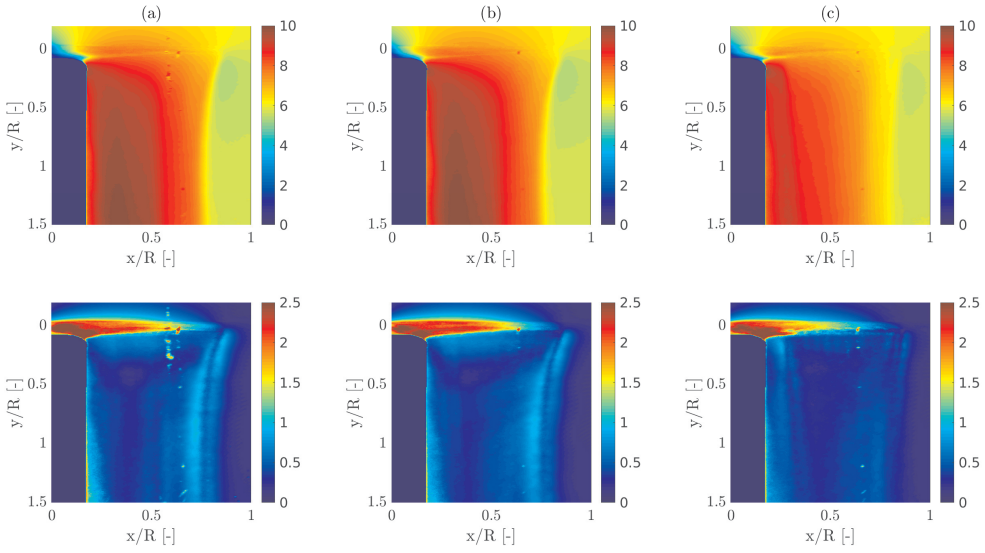

Figure 11. Mean velocity (top) and rms velocity (bottom) at $v = 6\,m/s$ and $\Omega = 5000\,RPM$. (a) represents the baseline propeller, (b) the b_1h_2 propeller and (c) the b_3h_3 propeller.

Again, the position of the maximum velocity in the slipstream for the b_3h_3 propeller is closer to the root with respect to the baseline and b_1h_2 propellers. Since the tip vortex is shed in the wake as soon as it is generated, the rms velocity does not show a significant increase at the rotor plane. However, the fluctuations associated with the traveling of the tip vortex in the wake are clearly visible and a considerable reduction is observed for the b_3h_3 propeller.

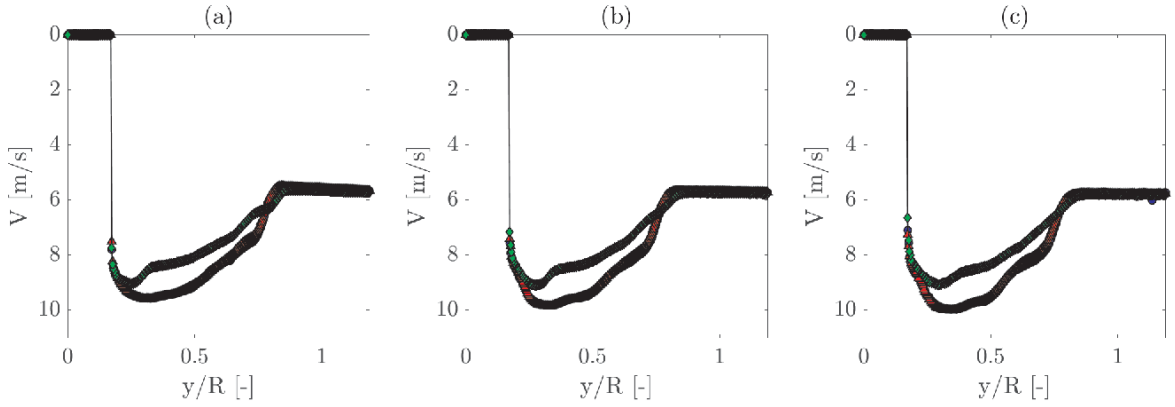

Figure 12. Mean velocity profiles at (a) $y/R = 0.5$, (b) $y/R = 1$ and (c) $y/R = 1.5$ for $v = 6\,m/s$ and $\Omega = 5000\,RPM$. The $\circ$ represents the baseline propeller, the $\triangle$ the b_1h_2 propeller and the $\diamond$ line the b_3h_3 propeller.

5. Conclusions

An experimental analysis on serrated trailing edge propeller has been performed in order to investigate their aerodynamic and aeroacoustic behaviour. 23 quiet propellers has been manufactured by employing a sawtooth pattern at the trailing edge of the blade, between all of them the two main interesting test cases has been object of further study in comparison with a reference one (i.e. a propeller without any acoustic optimization). The experimental tests have been carried out in hovering and advanced flight condition within an anechoic wind tunnel by means of load cell and microphones measurements. Moreover, to gain a better knowledge of the serration effect on the fluid dynamic fields a stereoscopic PIV has been performed for both the flight condition.

Results show that a sensible reduction in the noise footprint can be achieved. As already known in the literature, the longer the teeth the stronger the noise mitigation effect; the main drawback of serration is a reduction in the thrust coefficient for the STE propeller in respect to the baseline. This aspect suggests that a particular attention has be paid during the design process of quiet propeller in order to guarantee a proper thrust force generation. Furthermore, the noise source exhibits a strong directivity showing a "silent" region where the serrations has a major effect. Finally, noise reduction affects both tonal, this aspect requires a detailed study, and broadband components.

The mean velocity and rms velocity distribution highlight a lower wake velocity regarding the STE propeller in respect to the baseline and a lower tip vortex intensity. It is well-known that tip vortex is one of the main noise source for rotor, since the PIV shed light on the noise generation mechanism. Finally, the velocity profiles present two effects of serration; in particular, the maximum value of the induced velocity has been reduced for the serrated propeller (mostly regarding the b_3h_3 one) and also the velocity distribution in spanwise direction has been modified (moving the maximum to a position closer to the root).

References

[1] D. Floreano and R. J. Wood. Science, technology and the future of small autonomous drones. *Nature*, 521(7553):460–466, 2015.
[2] M. Cherney. Delivery drones cheer shoppers, annoy neighbors, scare dogs. *Wall Street Journal*, 2018.
[3] Gur and Rosen. Optimizing Electric Propulsion Systems for Unmanned Aerial Vehicles. *J. Aircr.*, 46(4):1340–1353, 2009.
[4] T. Pagliaroli, J.M. Moschetta, E. Benard, and C. Nana. Noise signature of a mav rotor in hover. *49th International Symposium of Applied Aerodynamics Lille, 24-25-26 March 2014*, pages 24–25, 2014.
[5] G. Sinibaldi and L. Marino. Experimental analysis on the noise of propellers for small UAV. *Appl. Acoust.*, 2013.
[6] Gur and Rosen. Design of a Quiet Propeller for an Electric Mini, 2009.
[7] D. JanakiRam and B. Scruggs. Investigation of performance, noise and detectability characteristics of small-scale remotely piloted vehicle /RPV/ propellers. *7th Aeroacoustics Conference*, 19(12):1052–1060, 1981.
[8] R. Serre, V. Chapin, J.M. Moschetta, and H. Fournier. Reducing the noise of micro–air vehicles in hover. *International Micro Air Vehicle Conference and Flight Competition*, pages 51–59, 2017.
[9] A. Leslie, K.C. Wong, and D. Auld. Broadband Noise Reduction on a mini-UAV Propeller. In *14th AIAA/CEAS Aeroacoustics Conference (29th AIAA Aeroacoustics Conference)*, 2008.
[10] P.A. Nelson and C.L. Morfey. Aerodynamic Sound Production. *J. Sound Vib.*, 79(2):263–289, 1981.
[11] Y. Rozenberg, M. Roger, and S. Moreau. Rotating Blade Trailing-Edge Noise: Experimental Validation of Analytical Model. *AIAA Journal*, 2010.
[12] T. Pagliaroli, P. Candeloro, R. Camussi, O. Giannini, R.Panciroli, and G. Bella. Aeroacoustic Study of small scale Rotors for mini Drone Propulsion: Serrated Trailing Edge Effect. *2018 AIAA/CEAS Aeroacoustics Conference*, 2018.
[13] P. Candeloro, R.E. Nargi, F. Patanè, and T. Pagliaroli. Experimental Analysis of Small-Scale Rotors with Serrated Trailing Edge for Quiet Drone Propulsion Experimental. *J. Phys.*, 2020.
[14] N.S. Zawodny, D.D. Boyd Jr, and C.L. Burley. Acoustic Characterization and Prediction of Representative, Small-Scale Rotary-Wing Unmanned Aircraft System Components . *72nd American Helicopter Society (AHS) Annual Forum; 17-19 May 2016; West Palm Beach, FL; United States*, 2016.
[15] E. Pang, A. Cambray, D. Rezgui, M. Azarpeyvand, and S.A. Showkat-Ali. Investigation Towards a Better Understanding of Noise Generation from UAV Propellers. In *2018 AIAA/CEAS Aeroacoustics Conference*, 2018.
[16] I.A. Clark, C.A. Daly, W. Devenport, W.N. Alexander, N. Peake, J.W. Jaworski, and S. Glegg. Bio-inspired canopies for the reduction of roughness noise. *J. Sound Vib.*, 2016.
[17] N. Peake. The aeroacoustics of the Owl. In *LNME*, 2016.
[18] J.W. Jaworski and N.Peake. Aerodynamic noise from a poroelastic edge with implications for the silent flight of owls. *J. Fluid Mech.*, 2013.
[19] F. Farassat and G.P. Succi. A review of propeller discrete frequency noise prediction technology with emphasis on two current methods for time domain calculations. *Top. Catal.*, 1980.
[20] N. Intravartolo, T. Sorrells, N. Ashkharian, and R. Kim. Attenuation of Vortex Noise Generated by UAV Propellers at Low Reynolds Numbers. In *55th AIAA Aerospace Sciences Meeting*, 2017.
[21] R.H. Schlinker and R.K. Amiet. Helicopter rotor trailing edge noise. *7th Aeroacoustics Conference*, page 2001, 1981.
[22] Y. Rozenberg, M. Roger, and S. Moreau. Fan blade trailing-edge noise prediction using rans simulations. *J. Acoust. Soc. Am.*, 123(5):5207–5212, 2008.
[23] G.M. Corcos. The structure of the turbulent pressure field in boundary-layer flows. *J. Fluid Mech.*, 18(3):353–378, 1964.
[24] T.P. Chong and A. Vathylakis. On the aeroacoustic and flow structures developed on a flat plate with a serrated sawtooth trailing edge. *J. Sound Vib.*, 2015.
[25] M. S. Howe. Noise produced by a sawtooth trailing edge. *The Journal of the Acoustical Society of America*, 90(1):482–487, 1991.
[26] A. Halimi, B.G. Marinus, and S. Larbi. Analytical prediction of broadband noise from mini-RPA propellers with serrated edges. *Int J Aeroacoust*, 18(4-5):517–535, 2019.
[27] A. Halimi, B.G. Marinus, and S. Larbi. Trailing edge noise of innovative mini-RPA propeller blades geometry. *2018 AIAA/CEAS Aeroacoustics Conference*, pages 1–14, 2018.
[28] Z. Ning and H. Hu. An Experimental Study on the Aerodynamics and Aeroacoustic Characteristics of Small Propellers. In *54th AIAA Aerospace Sciences Meeting*, 2016.
[29] B.W. McCormick. *Aerodynamics, Aeronautics, and Flight Mechanics*. 1995.
[30] G.J. Leishman. *Principles of helicopter aerodynamics with CD extra*. Cambridge university press, 2006.